

Temperature selective thermometry with sub-100 nanosecond time resolution using dressed-spin states in diamond

Jiwon Yun[‡], Kiho Kim[‡], Sungjoon Park and Dohun Kim^{}*

Department of Physics and Astronomy, and Institute of Applied Physics, Seoul National University, Seoul 08826, Korea

[‡] These authors contributed equally to this work.

^{}Corresponding author: dohunkim@snu.ac.kr*

ABSTRACT

Versatile nanoscale sensors that are susceptible to changes in a variety of physical quantities often exhibit limited selectivity. We propose a novel scheme based on microwave-dressed spin states for optically probed nanoscale temperature detection using diamond quantum sensors, which provides selective sensitivity to temperature changes. By combining this scheme with a continuous pump-probe scheme using ensemble nitrogen-vacancy centers in nanodiamonds, we demonstrate a sub-100-nanosecond temporal resolution with thermal sensitivity of $3.7 \text{ K} \cdot \text{Hz}^{-1/2}$ that is insensitive to variations in external magnetic fields on the order of 2 G. The presented results are favorable for the practical application of time-resolved nanoscale quantum sensing, where temperature imaging is required under fluctuating magnetic fields.

KEYWORDS: NV center, dressed state, nanodiamond, nanothermometry

Introduction

Sensing local temperatures with the high spatiotemporal resolution is an important technique that can be utilized in a wide range of fields, including electronics and biology ¹⁻⁴. Among recently developed time-resolved nanothermometers ⁵⁻⁹, the nitrogen-vacancy (NV) color centers in diamond have been highlighted as promising temperature sensors ¹⁰⁻¹⁷ that can be operated under ambient conditions and at room temperature based on their newly developed quantum sensing properties ^{18, 19}, together with the material's chemical inertness, high photostability, and biocompatibility ²⁰.

NV centers have spin-triplet ground states in which the magnetic quantum number $m_s = 0$ and $m_s = \pm 1$ sublevels are energetically separated by temperature T -dependent zero-field splitting ($D(T)$) due to crystal field ²¹⁻²³. The relative transition frequencies between sublevels are susceptible to changes in environmental factors such as magnetic fields ^{24, 25}, electric fields ^{26, 27}, strain ²⁸⁻³¹, and temperature ^{32, 33} meaning NV centers can serve as versatile nanoscale sensors. For primary sensing applications, many NV-center-based magnetometry techniques have been developed, including continuous wave optically detected magnetic resonance (cw-ODMR)-based ³⁴ methods, pulsed ODMR-based ³⁵ methods, and more advanced dynamical decoupling pulse-sequence-based magnetometry for improving spin coherence time and field sensitivity by reducing the interactions between NV centers and other adjacent spins, such as ¹³C nuclear spins ³⁶⁻³⁸.

Unlike magnetometry, NV-center-based thermometry utilizes energy level shifts related to direct changes in $D(T)$. Because the relative energy level difference is the only accessible

information in an experiment, the careful calibration or experimental fixing of environmental factors other than the desired sensing quantity is necessary. This is particularly problematic in thermometry, where magnetic-field-induced sublevel shifts often overwhelm temperature-related changes³². Several studies have proposed approaches to suppressing magnetic field effects. For example, pulse sequences such as the thermal echo, thermal Carr-Pucell-Meiboom-Gill sequence, and D-Ramsey sequence have been developed for high-temperature sensitivity^{12, 13}. Real-time monitoring methods have also been developed to reduce magnetic field effects^{14, 16, 17}. Although these studies have shown merit with carefully pre-calibrated settings, robustness to a wide range of field magnitudes and directions has not been demonstrated and existing methods often exhibited limited temporal resolution because a long phase accumulation time per sequence is required. Therefore, it is important to develop continuous measurement-based sequences that can be applied in non-zero external magnetic field environments.

Here, we propose and demonstrate an NV-center-based micron-scale time-resolved thermometry method using microwave-dressed spin states. In a dressed spin space³⁹⁻⁴¹, temperature-induced frequency shifts can be detected using net spin-zero eigenstates. Temperature information can be obtained by measuring up to six frequency components within the ODMR curve, making the proposed method applicable to real-time or time-resolved measurements. We demonstrate time-resolved temperature measurements with 10- μm spatial resolution and 50 ns temporal resolution using NV centers in nanodiamonds with natural tolerance to the varying magnitudes and directions of external magnetic fields¹³. When combined with well-developed independent magnetometry methods, the proposed method provides an effective route for a wide range of quantum sensing and chip-scale imaging applications for which selectivity and sensitivity to sensing quantities are both important.

Figure 1a presents a schematic of the proposed quantum sensing setup, where the NV centers in diamonds are subjected to microwave power-induced Joule heating of the coplanar waveguide (CPW), as well as an external magnetic field of arbitrary magnitude and direction. By ignoring the effects of the nitrogen or ^{13}C nuclear spins in diamond, the Hamiltonian can be described as (we adopt $\hbar=1$)

$$H_0 = D(T)S_z^2 + \gamma_e \mathbf{B} \cdot \mathbf{S} + E(S_x^2 - S_y^2), \quad (1)$$

where $\gamma_e = 2.8 \text{ MHz/G}$ is the gyromagnetic ratio of the electron spin, \mathbf{B} is the external magnetic field, E is the off-axial strain, and $S_i, i=x,y,z$ (\mathbf{S}) is the i^{th} component (vector) of spin-1 matrices with their NV axis set as the z -direction.

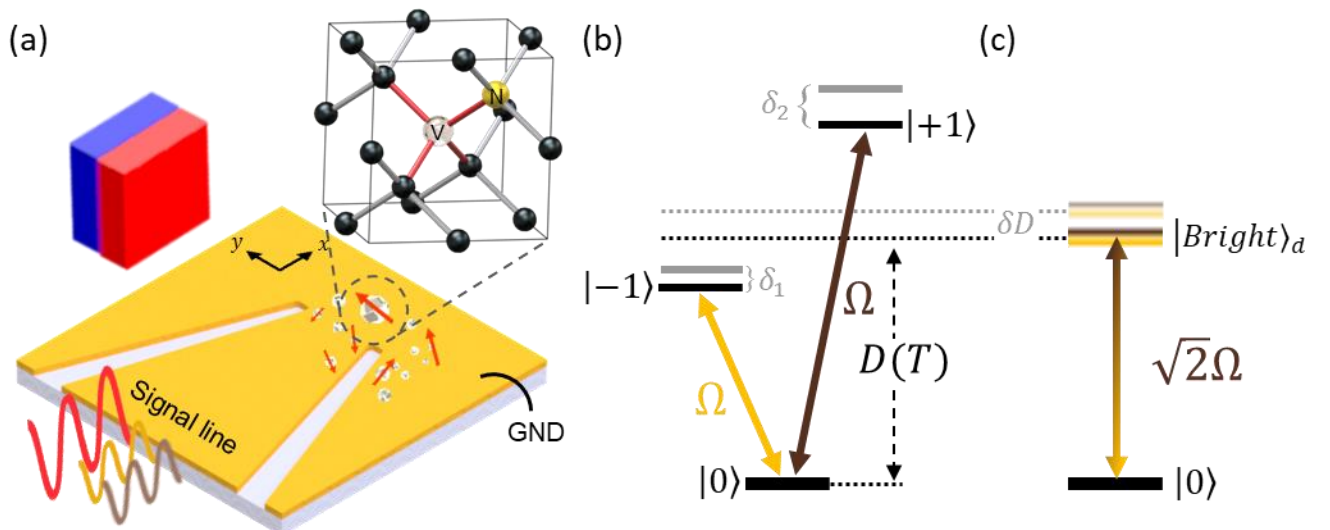


Figure 1. (a) Schematic of temperature measurement using NV centers in nanodiamonds under an arbitrary external magnetic field. The microwaves for spin state measurement and heating are

fed into the shorted-end coplanar waveguide (CPW) signal line. (b) The energy level of the NV center ground state, where D represents the zero-field splitting of the spin-triplet and Ω represents the Rabi oscillation frequency resonant to the $|0\rangle \leftrightarrow |\pm 1\rangle$ transition. (c) State transition between the $|Bright\rangle_d$ state in the dressed-state basis and $|0\rangle$ state when applying the microwave shown in (b).

As shown in Fig. 1b, typical quantum sensing measures changes in the transition frequency between bare spin states ($|0\rangle$, $|-1\rangle$, and $|+1\rangle$) by applying corresponding microwave pulses. By applying the double rotating frame approximation, the effects of small changes in $D(T)$ ($\delta D(T)$) and \mathbf{B} ($\delta \mathbf{B} = (\delta B_x, 0, \delta B_z)$) lead to a linear change in the frequencies, where $\delta_{1(2)} = (\delta D(T) - (+)\gamma_e \delta B_z) + 3 \frac{\gamma_e B_x}{D(T)} \gamma_e \delta B_x$. Therefore, extracting $D(T)$ information from the measurement of $\delta_{1(2)}$ requires prior knowledge regarding \mathbf{B} . A lack of this knowledge leads to significant temperature measurement errors based on the large sensitivity of NV centers to magnetic fields ($\gamma_e = 2.8$ MHz/G versus $dD/dT \sim 74$ kHz/K³²).

We address this issue by changing the eigenbasis to microwave-dressed spin states defined by $|0\rangle_d = |0\rangle$, $|Bright\rangle_d = (|+1\rangle + |-1\rangle)/\sqrt{2}$, and $|Dark\rangle_d = (|+1\rangle - |-1\rangle)/\sqrt{2}$, as shown in Fig. 1c. In the dressed spin state basis, the eigenstates exhibit nearly zero Zeeman splitting, opening a pathway for the selective measurement of temperature. Specifically, the Hamiltonian in the dressed basis becomes

$$H_{tot,d} = \begin{pmatrix} \delta_D & \sqrt{2}\Omega & \delta_B \\ \sqrt{2}\Omega & 0 & 0 \\ \delta_B & 0 & \delta_D \end{pmatrix}, \quad (2)$$

where Ω is the Rabi frequency, $\delta_D = \frac{\delta_1 + \delta_2}{2} \approx \delta D(T) + 3 \frac{\gamma_e B_x}{D(T)} \gamma_e \delta B_x \approx \delta D(T)$ is the response of

the energy level of the $|Bright\rangle_d$ and $|Dark\rangle_d$ state, and the coupling between the $|Bright\rangle_d$ and

$|Dark\rangle_d$ state is $\delta_B = \frac{\delta_2 - \delta_1}{2} \approx \gamma_e \delta B_z$ when $\gamma_e B_x \ll D(T)$. By directly driving $|0\rangle$ to $|Bright\rangle_d$,

the influence of the fluctuation δB_z is negligible in the strong driving regime $\delta_B \ll \sqrt{2}\Omega$ and the effects of the transverse field fluctuation δB_x are reduced by a factor of $3\gamma_e B_x / D(T)$.

Additionally, when the dressed spin state is used under an intermediate external magnetic field ($E \ll \gamma_e |\mathbf{B}|$), the energy levels become robust to changes in E . In Supporting Information S1, we describe this theoretical analysis in greater detail.

Results

We first validated the robustness of the dressed state to changes in the external magnetic field at a constant temperature using a single NV center in a type-Ib bulk diamond (See Supporting Information S2 for details). For this experiment, we applied a variable external magnetic field in a fixed arbitrary direction. The upper panel of Fig. 2a presents the ODMR obtained by sweeping a single microwave tone frequency. The two resonant peaks at ω_1 and ω_2 for the NV center represent energy level splitting between the $|0\rangle \leftrightarrow | -1 \rangle$ and $|0\rangle \leftrightarrow | +1 \rangle$ states.

We then measured the dressed state cw-ODMR (DS-ODMR) spectrum by applying two microwaves simultaneously with equal frequency detuning from ω_1 and ω_2 to the NV center to control it within its double rotating frame, as shown in Fig. 1a (bottom panel).

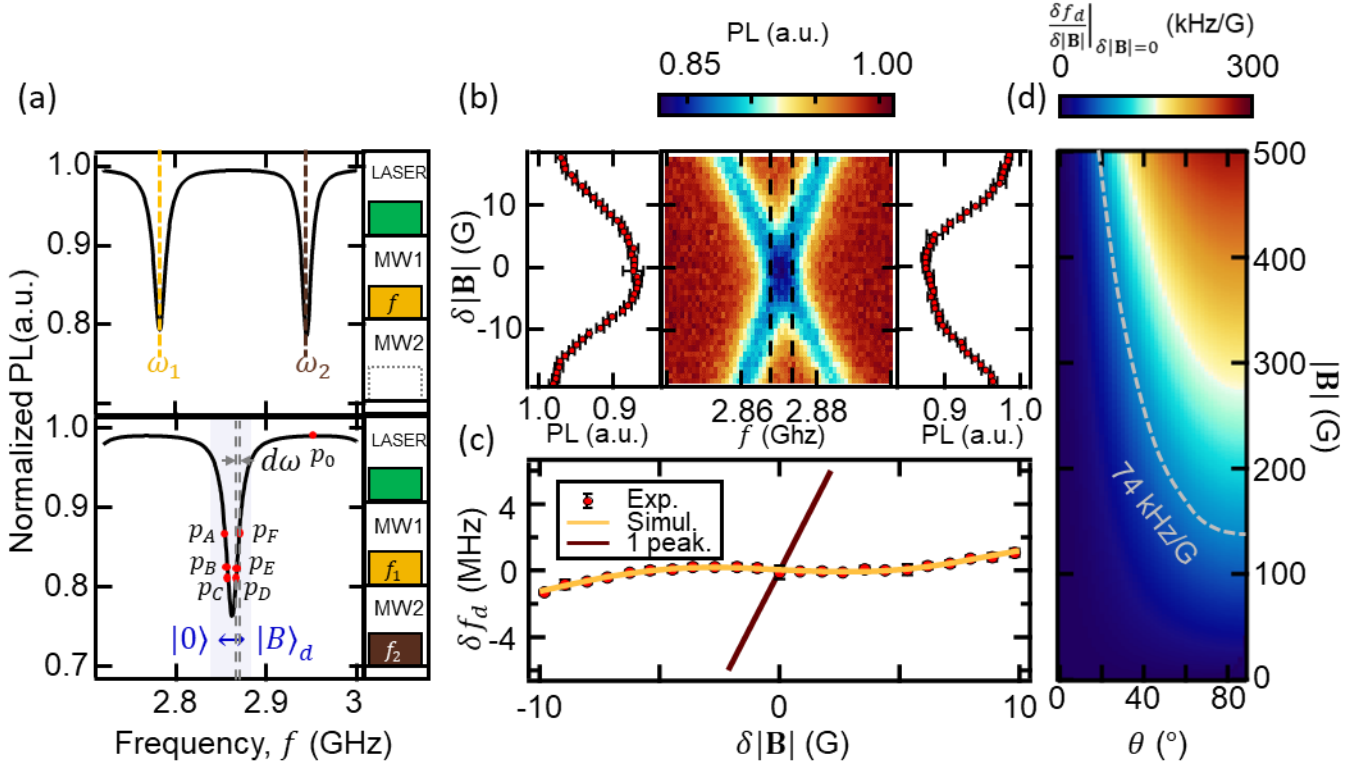


Figure 2 (a) The upper part shows the ODMR spectrum of a single NV center in a finite magnetic field obtained using the sequence on the right. The transition frequencies between $m_s = 0$ and $m_s = \pm 1$ are denoted as ω_1 and ω_2 , respectively. The lower part shows the dressed-state cw-ODMR spectrum measured by applying two microwaves (MW1, MW2) with a frequency difference of $\omega_2 - \omega_1$ simultaneously, as shown in the right pulse sequence. The center dip represents the resonance peak formed by the bright state of the MW dressed state. The x-axis of the ODMR spectra represents the average frequency of the two microwaves used in the

sequence. The red points represent the measurement frequencies used for thermometry, as described in the main text. (b) 2D image of the dressed-state cw-ODMR results while sweeping the external magnetic field. (c) Measured f_d changes at a fixed temperature depending on external magnetic field detuning. The red dots represent the change in f_d converted from fluorescence signals and the yellow line represents the simulated results for the DS-ODMR under the same conditions using QuTip. The brown line represents the converted frequency difference of the center frequency of a single peak in the single-microwave cw-ODMR. (d) Simulation results for

the attenuated $\left. \frac{\delta f_d}{\delta |\mathbf{B}|} \right|_{\delta |\mathbf{B}|=0}$ of the proposed method with changes in the strength and angle of the

external magnetic field. The grey dotted line represents the line at which $\left. \frac{\delta f_d}{\delta |\mathbf{B}|} \right|_{\delta |\mathbf{B}|=0} = 74$

kHz/G.³²

When sweeping the two microwave frequencies as $f_1 = f - (\omega_2 - \omega_1)/2$ and $f_2 = f + (\omega_2 - \omega_1)/2$ with a common center microwave frequency f , the resonance at $f_d = (\omega_1 + \omega_2)/2$ (double resonance with $f_1 = \omega_1$, $f_2 = \omega_2$) represents the transition between $|0\rangle \leftrightarrow |Bright\rangle_d$ states in the dressed state basis, where the variation in f_d is directly proportional to δ_D . Two methods were used for the extraction of δf_d induced by external perturbations. For a simple three-point measurement (the six-point method is discussed below), δf_d can be extracted as

$$\delta f_d = \frac{p_B - p_E}{p_B + p_E - 2p_0} \frac{\Gamma}{\sqrt{3}}, \quad (3)$$

where Γ is the linewidth of the DS-ODMR Lorentzian curve, and p_B , p_E , and p_0 are the measured photon counts at the center microwave frequencies $f_B = f_d - \Gamma/2\sqrt{3}$, $f_E = f_d + \Gamma/2\sqrt{3}$, and the f_0 that corresponds to the background photon counts (see Fig. 2a).¹⁷

The middle panel in Fig. 2b presents the DS-ODMR as a function of $\delta|\mathbf{B}|$ with respect to a reference field $|\mathbf{B}|$ of 47 G. As shown in the left and right panels of Fig. 2b, the measured photon counts $p_B(\delta|\mathbf{B}|)$ and $p_E(\delta|\mathbf{B}|)$ exhibit a plateau near $\delta|\mathbf{B}| = 0$, demonstrating robustness against magnetic field variation. When converted into f_d variation (Fig. 1c), the dressed state exhibits attenuation in f_d variation as a result of $\delta|\mathbf{B}|$ down to approximately 50 kHz/G, which is approximately 56 times smaller than 2.8 MHz/G of the bare spin states (Fig. 2c, brown solid line), which is consistent with the prediction given by Eq. (2). This result also agrees well with numerical simulations based on the QuTip package^{42, 43}. As $\delta|\mathbf{B}|$ increases, δ_B eventually becomes comparable to $\sqrt{2}\Omega$ and the $|0\rangle_d$ - $|Bright\rangle_d$ state subspace can no longer be considered to be decoupled from the $|Dark\rangle_d$ state, resulting in non-negligible deviations caused by $\delta|\mathbf{B}|$. Fig. 2d presents the numerical simulations (see Supporting Information S3 for details)

for the magnetic-field-induced error $\left. \frac{\delta f_d}{\delta|\mathbf{B}|} \right|_{\delta|\mathbf{B}|=0}$ as a function of the magnitude and orientation of

B. The gray dashed curve represents a contour of 74 kHz/G corresponding to 1 K/G when converted into temperature, demonstrating that the orientation and magnitude of the operating field for this method can vary widely while maintaining a sub-Kelvin magnetic field-induced temperature error.

We applied the dressed-state sensing method to ensemble NV centers to demonstrate time-resolved thermometry. Figure 3a presents dispersed nanodiamonds with an average diameter of 100 nm on top of a CPW on a cover glass substrate. From the single-tone ODMR curve with $|\mathbf{B}| = 190$ G, we selected the two peaks stemming from the NV ensembles whose axes are within approximately 29° with respect to the direction of \mathbf{B} to ensure temperature selectivity, as discussed above.⁴⁴ Temperature variation was induced by a 3- μ s-long microwave pulse with a carrier frequency of 2.8 GHz, power of 48 dBm, and repetition rate of 100 kHz applied to the CPW. To compensate for the fluctuation in linewidth, average fluorescence, and long-term drift, we introduced the six-point measurement method (Fig. 3b), which uses the measured photon counts from p_A to p_F at corresponding center frequencies f_A to f_F , as shown in Fig. 2a. We used the same two main points that were used for the center frequency calculation in Fig. 2 (p_B, p_E), but instead of obtaining the slope of the Lorentzian from a fixed Γ value, we calculated the slope of the Lorentzian for each measurement period using the additional four points (p_A, p_C, p_D, p_F).

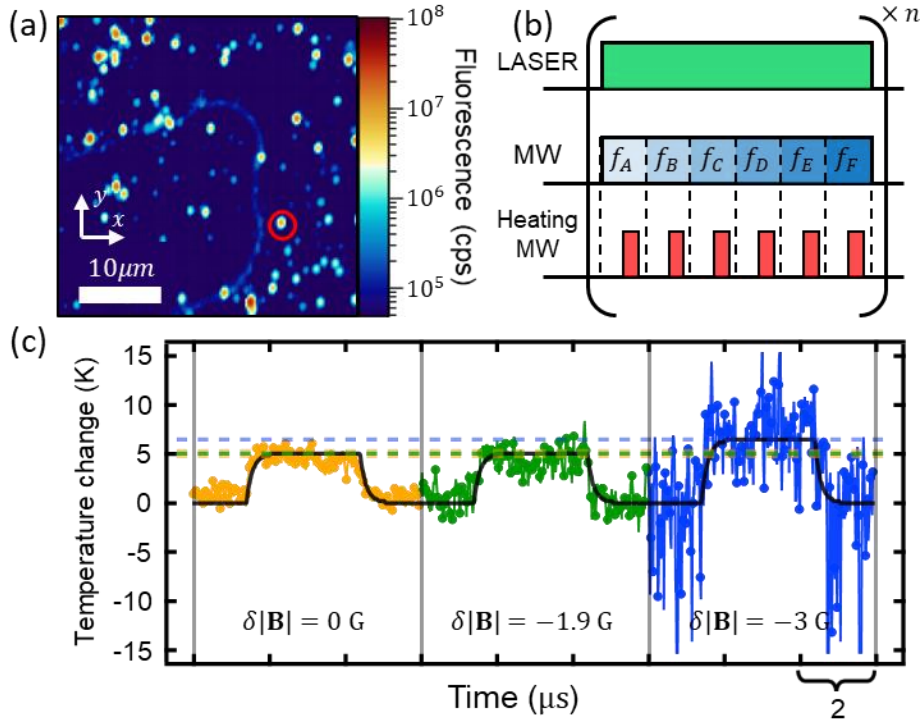


Figure 3. (a) Two-dimensional confocal scanning image of the NV centers in nanodiamonds dispersed on a cover glass with a shorted CPW fabricated on top. The temperature was measured at the marked NV center ensemble (red circle). (b) The microwave sequence used for pump-probe temperature measurement. (c) Time-resolved measurement results using the six-point DS-ODMR method under different levels of external magnetic field detuning $\delta|\mathbf{B}|$. Each color of the dashed lines represents a temperature change value at the end of the heating MW pulse. The overlaid black line represents the simulation results for the converted temperature when the six-point measurement method is applied to the temperature changes calculated by HFSS and Python (see Supporting Information S3 and S5 for details).

The temperature change can be extracted as (see Supporting Information S4 for details)

$$\delta T = \frac{p_B - p_D}{(p_A - p_C) - (p_D - p_F)} \frac{2d\omega}{dD/dT} \quad (4)$$

with a shot-noise-limited sensitivity of

$$\eta_T = 0.77 \frac{1}{dD/dT} \frac{\Gamma}{C_0} \frac{1}{\sqrt{R}}, \quad (5)$$

where C_0 is the luminescence contrast of the DS-ODMR curve and R is the measured photon count per second (cps). Figure 3c presents a comparison of the resultant time-resolved thermometry for different values of $\delta|\mathbf{B}|$. The results measured with no magnetic field detuning reveal a root-mean-squared (RMS) temperature fluctuation of approximately 0.6 K. Combining this result with the integration time for each data point of 43 s leads to a sensitivity of $3.7 \text{ K} \cdot \text{Hz}^{-1/2}$, which is above the shot-noise-limited sensitivity of $2.5 \text{ K} \cdot \text{Hz}^{-1/2}$ expected for this NV center ensemble. Therefore, a temperature change of approximately 5 K initiated by a pulsed microwave was measured with a signal-to-noise ratio (SNR) of approximately 8.3. Additionally, a rise time of approximately 300 ns can be resolved by our continuous-measurement-based time-resolved thermometry, where for the present setup, the time resolution is set by a 48 ns time step. As shown in the middle panel of Fig. 3c, the result is robust to $\delta|\mathbf{B}|$ up to approximately 2 G, demonstrating a systematic error of 0.1 K in the measured temperature change due to $\delta|\mathbf{B}|$ which is less than the RMS temperature fluctuation, which is in agreement with the QuTip simulation results of the six-point measurement method applied to the temperature simulation results represented by a black solid line. (see below for simulation details, see also Supporting Information S3 and S5.) This result is in agreement with the robust magnetic field range presented in Fig. 2. When $\delta|\mathbf{B}|$ is approximately 3 G, the systematic error is significant,

reflecting the deviation demonstrated in the dressed-state picture as discussed above.

Additionally, the SNR is less than 3 in this regime because the six-point measurement method becomes unstable when $\delta B_z \sim \sqrt{2}\Omega$.

We will now discuss spatiotemporally resolved thermometry. Under the same pulsed heating scheme, Fig. 4a presents three different NV centers distributed over the CPW, where the transient temperature increases over time differ, which can be inferred from the numerical simulations of the temperature distribution presented in Fig. 4b. The numerical simulations were performed using combinations of microwave loss calculations based on HFSS software and heat conduction calculations based on Fourier's law along the surface of a physical environment with a convection term using Python (see Supporting Information S5 for details). Figure 4c presents an overlay of the simulation results (solid and dashed curves) and experimental results (symbols) for the temperature changes during microwave heating. By applying the convection term

$Q_{\text{convection}} = h_{\text{convection}}(T - T_{\infty})$, where $h_{\text{convection}}$ is the convective heat transfer and T_{∞} is the temperature at the boundary, 26 °C for this experiment, the experimental result exhibits good agreement with $h_{\text{convection}} = 2 \times 10^8 \text{ W}/(\text{m}^2 \cdot \text{K})$. The results demonstrate that this method can be applied to various orientations of NV ensembles in a common setting, particularly under a common external magnetic field, which is made possible by the properties of the dressed state discussed above.

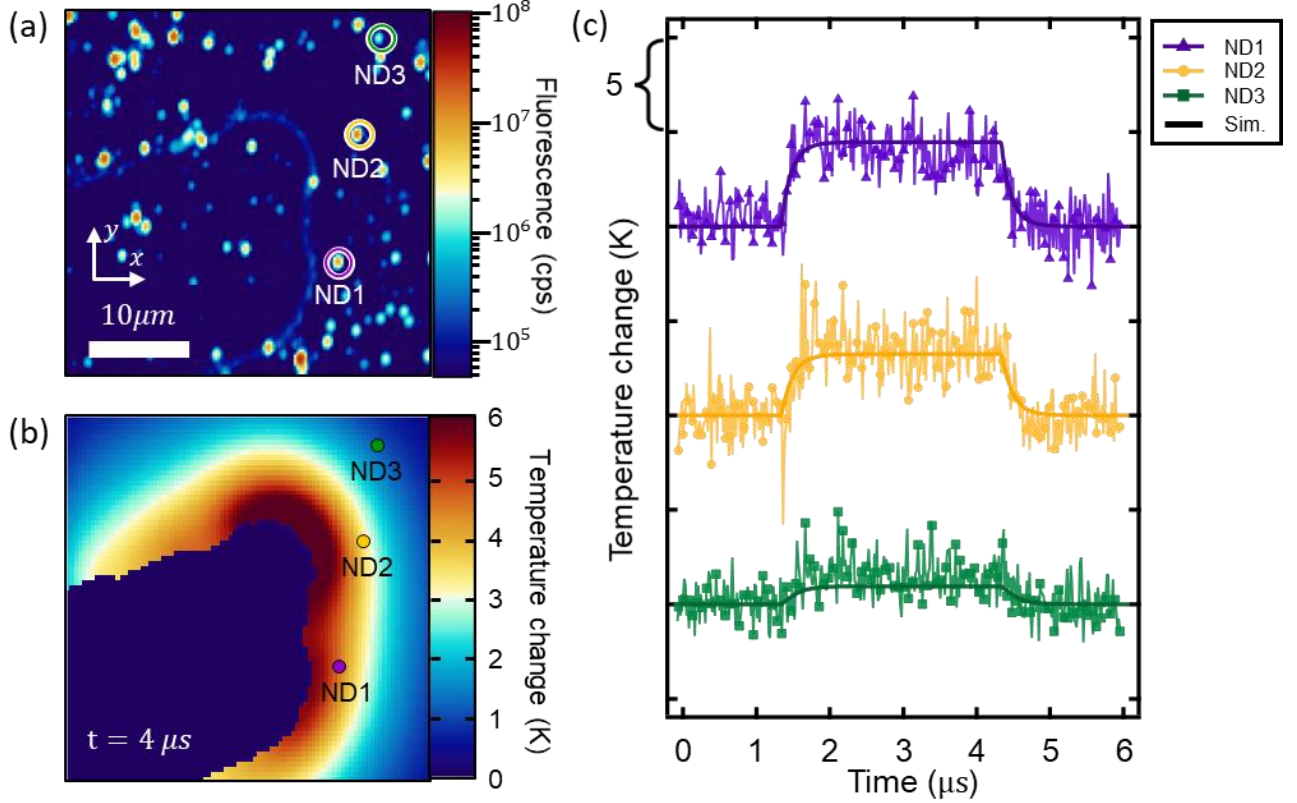


Figure 4. (a) Two-dimensional confocal scanning image of the NV centers in nanodiamonds dispersed on a gold CPW. The temperature was measured at the three marked NV center ensembles (colored circles). (b) Simulation results for the temperature distribution of the system when the temperature is saturated while the heating pulse is on. The colored dots represent the locations of the three nanodiamonds used for temperature measurement. (c) Overlaid experimental and simulation results for the time-resolved temperatures at the three measured NV centers.

In this work, we only evaluated the spatial resolution using nanodiamonds at a distance of approximately 10 μm apart from each other. In principle, the spatial resolution can be reduced to the diffraction limit of a confocal microscopy system, which could be implemented by increasing

the density of nanodiamonds on the CPW surface. When applying this method, a pre-selection process for NV ensembles is required because the resonance peaks from different axes may overlap, making it difficult to apply the DS-ODMR to a single axis independently. This limitation can be overcome by attaching a single nanodiamond particle to a probe and performing scanning for 2D temperature imaging. Even with these limitations, we measured the spatially resolved transient temperature of the CPW surface during the heating and cooling process on the gold surface with high thermal conductivity.

Discussion and Conclusions

We developed a novel thermometry method based on DS-ODMR measurements and pump-probe measurements, which provide high spatiotemporal resolution while maintaining robustness to external magnetic field environments. By using a dressed spin state basis for thermometry, we obtained a broad range of initial external magnetic fields that exhibited attenuated reactions to magnetic field fluctuations within the range satisfying $\delta_B \ll \sqrt{2}\Omega$. Additionally, the applicability of this basis to the cw-ODMR-type measurement scheme enables temperature measurement with high temporal resolution. By combining the DS-ODMR method with a pump-probe temperature measurement sequence and by adopting the six-point measurement method with time-tagged measurements for a reasonable total measurement time, we were able to resolve the transient temperature induced by a microwave pulse applied to a gold CPW with a time resolution of approximately 50 ns and temperature precision of 0.6 K. The insensitivity of the dressed spin state to external magnetic fields facilitated the application of this method to arbitrarily dispersed nanodiamond particles and allowed us to demonstrate

spatiotemporally resolved temperature measurement using several nanodiamonds on the CPW surface. Our thermometry method facilitates the measurement of time-resolved temperature using nanodiamonds in complex environments such as living cells, where aligning an external magnetic field to the NV center axis of each independent nanoparticle is difficult, as well as the characterization of nanoelectronic devices, where external magnetic fields fluctuate over time by varying the electric current. Therefore, the high temporal resolution and selective temperature sensitivity demonstrated here can be applied to the characterization of the transient thermal processes occurring in various nanoscale systems.

AUTHOR INFORMATION

Corresponding Author

Email: dohunkim@snu.ac.kr

ACKNOWLEDGMENT

This work was supported by the National Research Foundation of Korea (NRF) Grant funded by the Korean Government (MSIT) (No. 2018R1A2A3075438, No.2019M3E4A1080144, No.2019M3E4A1080145, and No.2019R1A5A1027055) and the Creative-Pioneering Researchers Program through Seoul National University (SNU).

REFERENCES

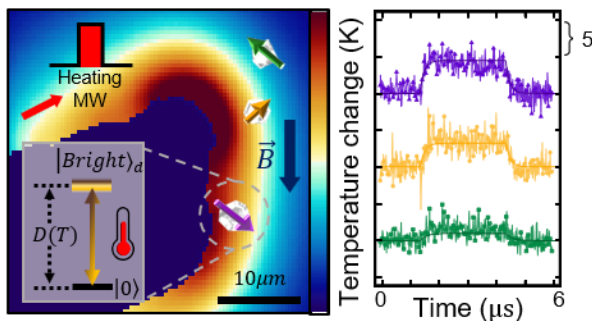
1. Yue, Y.; Wang, X., Nanoscale thermal probing. *Nano reviews* **2012**, 3, (1), 11586.
2. Brites, C. D.; Lima, P. P.; Silva, N. J.; Millán, A.; Amaral, V. S.; Palacio, F.; Carlos, L. D., Thermometry at the nanoscale. *Nanoscale* **2012**, 4, (16), 4799-4829.

3. Lancry, O.; Pichonat, E.; Réhault, J.; Moreau, M.; Aubry, R.; Gaquière, C., Development of Time-resolved UV Micro-Raman Spectroscopy to measure temperature in AlGaN/GaN HEMTs. *Solid-State Electronics* **2010**, 54, (11), 1434-1437.
4. Yoshida, K.; Nakanotani, H.; Adachi, C., Effect of Joule heating on transient current and electroluminescence in p-i-n organic light-emitting diodes under pulsed voltage operation. *Organic Electronics* **2016**, 31, 287-294.
5. Okabe, K.; Inada, N.; Gota, C.; Harada, Y.; Funatsu, T.; Uchiyama, S., Intracellular temperature mapping with a fluorescent polymeric thermometer and fluorescence lifetime imaging microscopy. *Nature communications* **2012**, 3, (1), 1-9.
6. Shang, L.; Stockmar, F.; Azadfar, N.; Nienhaus, G. U., Intracellular thermometry by using fluorescent gold nanoclusters. *Angewandte Chemie International Edition* **2013**, 52, (42), 11154-11157.
7. Donner, J. S.; Thompson, S. A.; Kreuzer, M. P.; Baffou, G.; Quidant, R., Mapping intracellular temperature using green fluorescent protein. *Nano letters* **2012**, 12, (4), 2107-2111.
8. Yang, J.-M.; Yang, H.; Lin, L., Quantum dot nano thermometers reveal heterogeneous local thermogenesis in living cells. *ACS nano* **2011**, 5, (6), 5067-5071.
9. Vetrone, F.; Naccache, R.; Zamarrón, A.; Juarranz de la Fuente, A.; Sanz-Rodríguez, F.; Martínez Maestro, L.; Martín Rodriguez, E.; Jaque, D.; García Solé, J.; Capobianco, J. A., Temperature sensing using fluorescent nanothermometers. *ACS nano* **2010**, 4, (6), 3254-3258.
10. Plakhotnik, T.; Doherty, M. W.; Cole, J. H.; Chapman, R.; Manson, N. B., All-optical thermometry and thermal properties of the optically detected spin resonances of the NV-center in nanodiamond. *Nano letters* **2014**, 14, (9), 4989-4996.
11. Fedotov, I.; Blakley, S.; Serebryannikov, E.; Safronov, N.; Velichansky, V.; Scully, M.; Zheltikov, A., Fiber-based thermometry using optically detected magnetic resonance. *Applied Physics Letters* **2014**, 105, (26), 261109.
12. Toyli, D. M.; Charles, F.; Christle, D. J.; Dobrovitski, V. V.; Awschalom, D. D., Fluorescence thermometry enhanced by the quantum coherence of single spins in diamond. *Proceedings of the National Academy of Sciences* **2013**, 110, (21), 8417-8421.
13. Neumann, P.; Jakobi, I.; Dolde, F.; Burk, C.; Reuter, R.; Waldherr, G.; Honert, J.; Wolf, T.; Brunner, A.; Shim, J. H., High-precision nanoscale temperature sensing using single defects in diamond. *Nano letters* **2013**, 13, (6), 2738-2742.
14. Kucsko, G.; Maurer, P. C.; Yao, N. Y.; Kubo, M.; Noh, H. J.; Lo, P. K.; Park, H.; Lukin, M. D., Nanometre-scale thermometry in a living cell. *Nature* **2013**, 500, (7460), 54-58.
15. Singam, S. K.; Nesladek, M.; Goovaerts, E., Nitrogen-vacancy nanodiamond based local thermometry using frequency-jump modulation. *Nanotechnology* **2019**, 31, (10), 105501.
16. Fujiwara, M.; Sun, S.; Dohms, A.; Nishimura, Y.; Suto, K.; Takezawa, Y.; Oshimi, K.; Zhao, L.; Sadzak, N.; Umehara, Y.; Teki, Y.; Komatsu, N.; Benson, O.; Shikano, Y.; Kage-Nakadai, E., Real-time nanodiamond thermometry probing in vivo thermogenic responses. *Science Advances* **2020**, 6, (37), eaba9636.
17. Tzeng, Y.-K.; Tsai, P.-C.; Liu, H.-Y.; Chen, O. Y.; Hsu, H.; Yee, F.-G.; Chang, M.-S.; Chang, H.-C., Time-resolved luminescence nanothermometry with nitrogen-vacancy centers in nanodiamonds. *Nano letters* **2015**, 15, (6), 3945-3952.
18. Schirhagl, R.; Chang, K.; Loretz, M.; Degen, C. L., Nitrogen-Vacancy Centers in Diamond: Nanoscale Sensors for Physics and Biology. *Annual Review of Physical Chemistry* **2014**, 65, (1), 83-105.

19. Barry, J. F.; Schloss, J. M.; Bauch, E.; Turner, M. J.; Hart, C. A.; Pham, L. M.; Walsworth, R. L., Sensitivity optimization for NV-diamond magnetometry. *Reviews of Modern Physics* **2020**, 92, (1), 015004.
20. Alkahtani, M. H.; Alghannam, F.; Jiang, L.; Almethen, A.; Rampersaud, A. A.; Brick, R.; Gomes, C. L.; Scully, M. O.; Hemmer, P. R., Fluorescent nanodiamonds: past, present, and future. *Nanophotonics* **2018**, 7, (8), 1423-1453.
21. Doherty, M. W.; Manson, N. B.; Delaney, P.; Hollenberg, L. C. L., The negatively charged nitrogen-vacancy centre in diamond: the electronic solution. *New Journal of Physics* **2011**, 13, (2), 025019.
22. Maze, J. R.; Gali, A.; Togan, E.; Chu, Y.; Trifonov, A.; Kaxiras, E.; Lukin, M. D., Properties of nitrogen-vacancy centers in diamond: the group theoretic approach. *New Journal of Physics* **2011**, 13, (2), 025025.
23. Ivády, V.; Simon, T.; Maze, J. R.; Abrikosov, I. A.; Gali, A., Pressure and temperature dependence of the zero-field splitting in the ground state of NV centers in diamond: A first-principles study. *Physical Review B* **2014**, 90, (23), 235205.
24. Balasubramanian, G.; Chan, I.; Kolesov, R.; Al-Hmoud, M.; Tisler, J.; Shin, C.; Kim, C.; Wojcik, A.; Hemmer, P. R.; Krueger, A., Nanoscale imaging magnetometry with diamond spins under ambient conditions. *Nature* **2008**, 455, (7213), 648-651.
25. Hong, S.; Grinolds, M. S.; Pham, L. M.; Le Sage, D.; Luan, L.; Walsworth, R. L.; Yacoby, A., Nanoscale magnetometry with NV centers in diamond. *MRS bulletin* **2013**, 38, (2), 155-161.
26. Dolde, F.; Fedder, H.; Doherty, M. W.; Nöbauer, T.; Rempp, F.; Balasubramanian, G.; Wolf, T.; Reinhard, F.; Hollenberg, L. C.; Jelezko, F., Electric-field sensing using single diamond spins. *Nature Physics* **2011**, 7, (6), 459-463.
27. Dolde, F.; Doherty, M. W.; Michl, J.; Jakobi, I.; Naydenov, B.; Pezzagna, S.; Meijer, J.; Neumann, P.; Jelezko, F.; Manson, N. B., Nanoscale detection of a single fundamental charge in ambient conditions using the NV- center in diamond. *Physical review letters* **2014**, 112, (9), 097603.
28. Ovartchaiyapong, P.; Lee, K. W.; Myers, B. A.; Jayich, A. C. B., Dynamic strain-mediated coupling of a single diamond spin to a mechanical resonator. *Nature Communications* **2014**, 5, (1), 4429.
29. Teissier, J.; Barfuss, A.; Appel, P.; Neu, E.; Maletinsky, P., Strain Coupling of a Nitrogen-Vacancy Center Spin to a Diamond Mechanical Oscillator. *Physical Review Letters* **2014**, 113, (2), 020503.
30. Barfuss, A.; Teissier, J.; Neu, E.; Nunnenkamp, A.; Maletinsky, P., Strong mechanical driving of a single electron spin. *Nature Physics* **2015**, 11, (10), 820-824.
31. Udvarhelyi, P.; Shkolnikov, V. O.; Gali, A.; Burkard, G.; Pályi, A., Spin-strain interaction in nitrogen-vacancy centers in diamond. *Physical Review B* **2018**, 98, (7), 075201.
32. Acosta, V. M.; Bauch, E.; Ledbetter, M. P.; Waxman, A.; Bouchard, L.-S.; Budker, D., Temperature dependence of the nitrogen-vacancy magnetic resonance in diamond. *Physical review letters* **2010**, 104, (7), 070801.
33. Chen, X.-D.; Dong, C.-H.; Sun, F.-W.; Zou, C.-L.; Cui, J.-M.; Han, Z.-F.; Guo, G.-C., Temperature dependent energy level shifts of nitrogen-vacancy centers in diamond. *Applied Physics Letters* **2011**, 99, (16), 161903.
34. Gruber, A.; Dräbenstedt, A.; Tietz, C.; Fleury, L.; Wrachtrup, J.; Von Borczyskowski, C., Scanning confocal optical microscopy and magnetic resonance on single defect centers. *Science* **1997**, 276, (5321), 2012-2014.

35. Dréau, A.; Lesik, M.; Rondin, L.; Spinicelli, P.; Arcizet, O.; Roch, J. F.; Jacques, V., Avoiding power broadening in optically detected magnetic resonance of single NV defects for enhanced dc magnetic field sensitivity. *Physical Review B* **2011**, 84, (19), 195204.
36. Grinolds, M. S.; Hong, S.; Maletinsky, P.; Luan, L.; Lukin, M. D.; Walsworth, R. L.; Yacoby, A., Nanoscale magnetic imaging of a single electron spin under ambient conditions. *Nature Physics* **2013**, 9, (4), 215-219.
37. Maze, J. R.; Stanwix, P. L.; Hodges, J. S.; Hong, S.; Taylor, J. M.; Cappellaro, P.; Jiang, L.; Dutt, M. G.; Togan, E.; Zibrov, A., Nanoscale magnetic sensing with an individual electronic spin in diamond. *Nature* **2008**, 455, (7213), 644-647.
38. Mamin, H.; Kim, M.; Sherwood, M.; Rettner, C.; Ohno, K.; Awschalom, D.; Rugar, D., Nanoscale nuclear magnetic resonance with a nitrogen-vacancy spin sensor. *Science* **2013**, 339, (6119), 557-560.
39. Xu, X.; Wang, Z.; Duan, C.; Huang, P.; Wang, P.; Wang, Y.; Xu, N.; Kong, X.; Shi, F.; Rong, X.; Du, J., Coherence-Preserved Quantum Gate by Continuous Dynamical Decoupling in Diamond. *Physical Review Letters* **2012**, 109, (7), 070502.
40. Mamin, H. J.; Sherwood, M. H.; Kim, M.; Rettner, C. T.; Ohno, K.; Awschalom, D. D.; Rugar, D., Multipulse Double-Quantum Magnetometry with Near-Surface Nitrogen-Vacancy Centers. *Physical Review Letters* **2014**, 113, (3), 030803.
41. Myers, B. A.; Ariyaratne, A.; Jayich, A. C. B., Double-Quantum Spin-Relaxation Limits to Coherence of Near-Surface Nitrogen-Vacancy Centers. *Physical Review Letters* **2017**, 118, (19), 197201.
42. Johansson, J. R.; Nation, P. D.; Nori, F., QuTiP 2: A Python framework for the dynamics of open quantum systems. *Computer Physics Communications* **2013**, 184, (4), 1234-1240.
43. Johansson, J. R.; Nation, P. D.; Nori, F., QuTiP: An open-source Python framework for the dynamics of open quantum systems. *Computer Physics Communications* **2012**, 183, (8), 1760-1772.
44. Maertz, B. J.; Wijnheijmer, A. P.; Fuchs, G. D.; Nowakowski, M. E.; Awschalom, D. D., Vector magnetic field microscopy using nitrogen vacancy centers in diamond. *Applied Physics Letters* **2010**, 96, (9), 092504.

For Table of Contents Only



Temperature-selective thermometry with sub-100-nanosecond time resolution using dressed-spin states in diamond

Jiwon Yun[†], Kiho Kim[†], Sungjoon Park and Dohun Kim^{*}

Department of Physics and Astronomy, and Institute of Applied Physics, Seoul National University, Seoul 08826, Korea

[†] These authors contributed equally to this work.

*Corresponding author: dohunkim@snu.ac.kr

Supplementary Information

1. Theoretical analysis on the dressed-spin states

The Hamiltonian of the NV center under arbitrary external magnetic field is given by,

$$H_0 = D(T)S_z^2 + \gamma_e \mathbf{B} \cdot \mathbf{S} + E(S_x^2 - S_y^2) \quad (\text{S1})$$

where $D(T)$ is the zero-field splitting of the NV center, γ_e is the gyromagnetic ratio of the electron spin, \mathbf{B} is the external magnetic field, and \mathbf{S} is the vector form of spin-1 matrices, and E is the off-axial strain. In matrix form,

$$H_0 = \begin{pmatrix} D(T) + \gamma_e B_z & \gamma_e B_x & E \\ \gamma_e B_x & 0 & \gamma_e B_x \\ E & \gamma_e B_x & D(T) - \gamma_e B_z \end{pmatrix} \quad (\text{S2})$$

where B_z is the magnetic field component parallel to the NV center axis and B_x is the perpendicular component. For the intermediate $|B|$ ranging $E \ll |B| \ll D(T)$, since the effect of E is negligible compared to combined energy scale set by the zero field and external magnetic field terms in the Hamiltonian (see Supplementary Fig. S1), the Hamiltonian can be approximated as

$$H_0 = \begin{pmatrix} D(T) + \gamma_e B_z & \gamma_e B_x & 0 \\ \gamma_e B_x & 0 & \gamma_e B_x \\ 0 & \gamma_e B_x & D(T) - \gamma_e B_z \end{pmatrix} \quad (S3)$$

and when this Hamiltonian is diagonalized, it can be approximated as

$$H_{diag} \sim \begin{pmatrix} D(T) + \gamma_e B_z + \frac{1}{2} \frac{\gamma_e B_x}{D(T)} \gamma_e B_x & 0 & 0 \\ 0 & -\frac{\gamma_e B_x}{D(T)} \gamma_e B_x & 0 \\ 0 & 0 & D(T) - \gamma_e B_z + \frac{1}{2} \frac{\gamma_e B_x}{D(T)} \gamma_e B_x \end{pmatrix} \quad (S4)$$

up to the order of $O((\gamma_e |B| / D)^3)$. We set the eigenbasis of the diagonalized Hamiltonian as $|+1\rangle$, $|0\rangle$, and $| -1\rangle$.

With external microwaves $H_{MW1} = \mathbf{\Omega}_1 \cdot \mathbf{S} \cos(\omega_1 t)$, $H_{MW2} = \mathbf{\Omega}_2 \cdot \mathbf{S} \cos(\omega_2 t)$, the total Hamiltonian in the doubly rotating frame becomes,

$$H_{tot} = \begin{pmatrix} \lambda_{(+)} - \omega_2 & \Omega_{1,xy} & 0 \\ \Omega_{1,xy} & 0 & \Omega_{2,xy} \\ 0 & \Omega_{2,xy} & \lambda_{(-)} - \omega_1 \end{pmatrix} \quad (S5)$$

where $\lambda_{(\pm)} \sim D(T) \pm \gamma_e B_z + \frac{3}{2} \frac{\gamma_e B_x}{D(T)} \gamma_e B_x + O\left(\left(\frac{\gamma_e |\mathbf{B}|}{D(T)}\right)^3\right)$ is the energy level splitting in each of the subspaces, ω_1, ω_2 is the microwave frequency applied to the $|0\rangle - |-1\rangle$ subspace and $|0\rangle - |+1\rangle$ subspace with the resonant condition is $\omega_1 = \lambda_{(-)}$ and $\omega_2 = \lambda_{(+)}$, and $\Omega_{1,xy} (\Omega_{2,xy})$ is the amplitude perpendicular to the quantization axis of each subspace of the microwave with frequency $\omega_1 (\omega_2)$. For the temperature measurement method in this study, we tune the perpendicular amplitude so that $\Omega_{1,xy} = \Omega_{2,xy} = \Omega$.

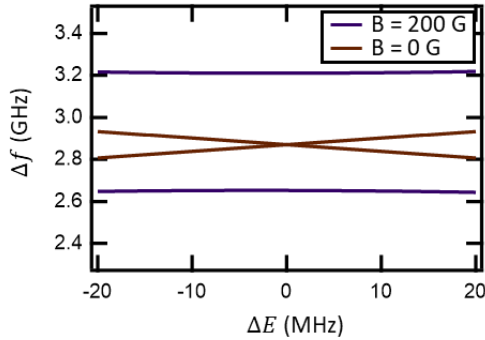
With detuning in $D(T)$ and \mathbf{B} corresponding to changes in environmental factors, the Hamiltonian becomes,

$$H_{tot} = \begin{pmatrix} \delta D(T) + \gamma_e \delta B_z + 3 \frac{\gamma_e B_x}{D(T)} \gamma_e \delta B_x + d\omega & \Omega & 0 \\ \Omega & 0 & \Omega \\ 0 & \Omega & \delta D(T) - \gamma_e \delta B_z + 3 \frac{\gamma_e B_x}{D(T)} \gamma_e \delta B_x + d\omega \end{pmatrix} \quad (S6)$$

Moving to the dressed spin state basis, the Hamiltonian becomes

$$H_{tot,d} = \begin{pmatrix} \delta D(T) + 3 \frac{\gamma_e B_x}{D(T)} \gamma_e \delta B_x + d\omega & \sqrt{2}\Omega & \gamma_e \delta B_z \\ \sqrt{2}\Omega & 0 & 0 \\ \gamma_e \delta B_z & 0 & \delta D(T) + 3 \frac{\gamma_e B_x}{D(T)} \gamma_e \delta B_x + d\omega \end{pmatrix} \quad (S7)$$

which is the result used in the main text.



Supplementary Figure S1. Energy level difference of the spin transitions under change of E . The energy level splitting becomes flat when an external magnetic field on the order of 100 G is present.

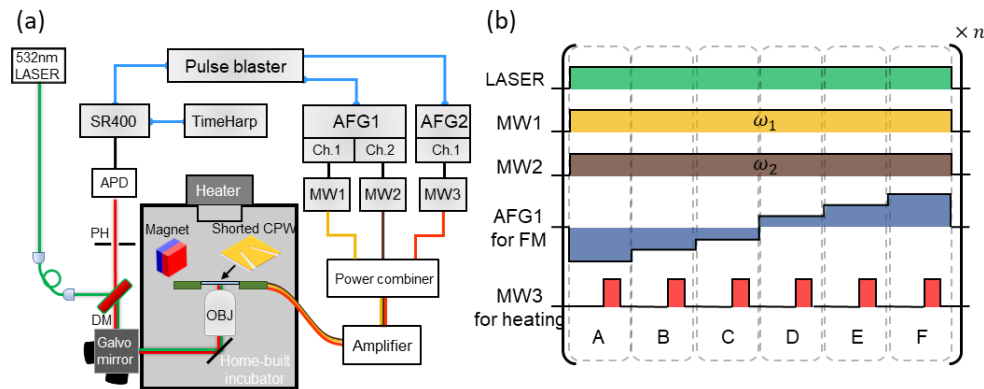
2. Experimental setup

We carried out the experiments in a homebuilt confocal microscope as schematically shown in Supplementary Fig. S2a. A green laser (CNI, MLL-III-532-200mW) is used for the measurement of the pulsed spin resonance characteristics of NV centers. The fluorescence emitted from NV centers is detected by an avalanche photodiode (APD, Excelitas, SPCM-AQRH-14-FC) which is connected to a two-channel gated photon counter (Stanford Research Systems, SR400). The external magnetic field was applied by locating a neodymium magnet fixed to a 3-axis stage around the diamond sample. The magnitude of the external magnetic field was varied by moving the 3-axis stage. To manipulate the electron spin state in the dressed frame, two driving microwaves are generated by signal generators (Stanford Research Systems, SG396 and SG394), which are gated by two arbitrary function generators (AFGs) (Tektronix, AFG3252) and applied to the NV centers simultaneously. The microwave pulses amplified by a high-power microwave amplifier (Mini-Circuits, ZHL-16W-43+) are fed to a coplanar waveguide (CPW) fabricated on a coverslip. We prepared a type-Ib bulk diamond (Element 6) for external magnetic field reaction analysis using a

single NV center and nanodiamonds with an average diameter of 100 nm (Adamas) dispersed on top of CPW for spatiotemporally resolved temperature-selective thermometry measurements.

In the time-resolved measurement, both the green laser and the microwaves from the two signal generators are applied continuously as shown in Supplementary Fig. S2b.

The output photons from the NV center are measured continuously using a time-tagged photon counting module (PicoQuant, TimeHarp 260 NANO). To measure the fluorescence at the 6 microwave frequencies of the Lorentzian curve, the analog frequency modulation mode is used in both signal generators and the input analog waveform was generated using the arbitrary waveform generator. The frequency modulation deviation we used was 16 MHz and the frequency modulation bandwidth was 100 kHz. Considering frequency switching time about 3.5 μ s, the first 4 μ s of data for each frequency measurement are discarded.



Supplementary Figure S2. Experimental setup (a) Schematic setup for confocal microscopy and microwave setup. (b) Laser and microwave pulse sequence used for time-resolved measurement.

3. QuTip simulation of the dressed state cw-ODMR results

Quantum dynamics of the dressed spin-states were simulated using the QuTip package in written python. The fluorescence of the ODMR measurement sequence was simulated using the ‘*mesolve*’ function in QuTip, which solves the master equation,

$$\frac{d\rho}{dt} = -i[H_{tot,d}, \rho] + \sum (L\rho L^\dagger - \frac{1}{2}\{L^\dagger L, \rho\}) \quad (\text{S8})$$

with the Hamiltonian of Eq. S7, where ρ is the system density operator. We used the Lindblad operator

$$L_{-1}^{gl} = \sqrt{\Gamma_{gl}} |0\rangle\langle -1|, \quad L_{+1}^{gl} = \sqrt{\Gamma_{gl}} |0\rangle\langle +1| \quad (\text{S9})$$

where Γ_{gl} is the decay rate coming from the green laser to reproduce the effect of the laser in the cw-ODMR measurement sequence. To simulate realistic cw-ODMR results, the master equation was calculated long enough for the quantum state to reach equilibrium ($\tau_{ODMR} > 1/\Gamma_{gl}$). We used $\Gamma_{gl} \sim 10$ MHz and the time range we used to solve the master equation to obtain the ODMR fluorescence was $\tau_{ODMR} \sim 10$ μ s to match the experimental pulse repetition period.

4. The 6-point method for dressed state thermometry

By characterizing the Lorentzian resonance curve $L(f)$ of the dressed state cw-ODMR as a function of applied microwave frequency f , we convert the change in the photoluminescence (PL) of the six center frequencies $f_{A(B,C,D,E,F)}$ of the two applied microwaves into temperature difference. We choose these frequencies as follows.

$$f_A = (\omega_1 + \omega_2)/2 - \Gamma/2\sqrt{3} - d\omega,$$

$$f_B = (\omega_1 + \omega_2)/2 - \Gamma/2\sqrt{3},$$

$$f_C = (\omega_1 + \omega_2)/2 - \Gamma/2\sqrt{3} + d\omega, \quad (S10)$$

$$f_D = (\omega_1 + \omega_2)/2 + \Gamma/2\sqrt{3} - d\omega,$$

$$f_E = (\omega_1 + \omega_2)/2 + \Gamma/2\sqrt{3},$$

$$f_F = (\omega_1 + \omega_2)/2 + \Gamma/2\sqrt{3} + d\omega,$$

where Γ is the linewidth of $L(f)$ and $d\omega$ is a detuning given to obtain the slope of the Lorentzian.

The PL at each frequency can be approximated as,

$$\begin{aligned} p_A &= p_{B,0} + \frac{dL}{df} \Big|_{f=f_B} \left(\frac{dD}{dT} \delta T - d\omega \right) \\ p_B &= p_{B,0} + \frac{dL}{df} \Big|_{f=f_B} \left(\frac{dD}{dT} \delta T \right) \\ p_C &= p_{B,0} + \frac{dL}{df} \Big|_{f=f_B} \left(\frac{dD}{dT} \delta T + d\omega \right) \\ p_D &= p_{B,0} - \frac{dL}{df} \Big|_{f=f_B} \left(\frac{dD}{dT} \delta T - d\omega \right) \\ p_E &= p_{B,0} - \frac{dL}{df} \Big|_{f=f_B} \left(\frac{dD}{dT} \delta T \right) \\ p_F &= p_{B,0} - \frac{dL}{df} \Big|_{f=f_B} \left(\frac{dD}{dT} \delta T + d\omega \right) \end{aligned} \quad (S11)$$

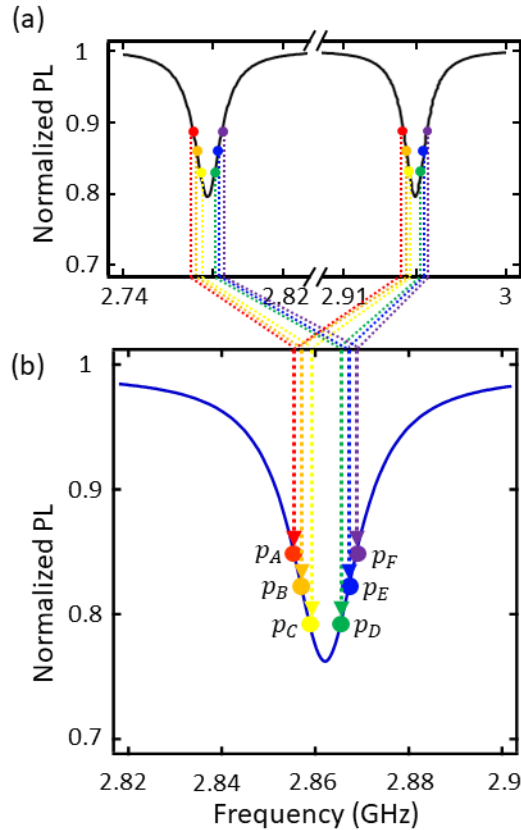
where $p_{A(B,C,D,E,F)}$ is the measured PL using $f_{A(B,C,D,E,F)}$ (see Supplementary Fig. S3), $p_{B,0}$ is the PL at the initial temperature at f_B , $dD/dT \sim 74$ kHz/K near 300 K, and δT is the change in the temperature. Solving these equations, we obtain temperature conversion formula as,

$$\delta T = \frac{p_B - p_E}{(p_C - p_A)/2 - (p_F - p_D)/2} \frac{d\omega}{dD/dT} \quad (S12)$$

In addition, the shot-noise limited sensitivity of this method can be calculated from the slope of the Lorentzian curve as

$$\eta_T = 0.77 \frac{1}{dD/dT} \frac{\Gamma}{C_0} \frac{1}{\sqrt{R}} \quad (\text{S13})$$

where C_0 is the contrast of the dressed state cw-ODMR, and R is the measured photon count per second.



Supplementary Figure S1 (a) Microwave frequencies applied to the NV center in the 6 point measurement for the DS-ODMR. (b) The corresponding points represented in the DS-ODMR curve.

5. Temperature simulations

Dielectric loss calculation

To confirm the measured time-resolved temperature measurement, we conducted a numerical simulation of the temperature change. Based on the optical microscope image of the CPW, we replicated the geometrical structure. To describe the temperature change at the shorted-end of the CPW, the power losses attributed to the conductor and dielectric losses can be considered. We first calculated the power loss generated from the tapered and shorted coplanar waveguide design using the High-Frequency Structure Simulator (HFSS, ANSYS software), a simulator based on the finite element method, and obtained the surface loss density on the gold surface. The volume loss density of the substrate is neglected in this work as we are dealing with materials of low loss-tangent.

Numerical heat transfer simulation

Based on the calculated heat generation, we ran a numerical simulation using python. We designed a program to solve the 2-dimension partial differential equation with the Neumann boundary condition based on Fourier's law using discrete grids. The main equation used is

$$\begin{aligned}
 T(x, y, t + dt) = & T(x, y, t) - \frac{dt}{\rho(x, y) C_{sp}(x, y)} \left(\right. \\
 & \sigma(x, y) \frac{(T(x, y, t) - T_{-x}(x, y, t))}{(dx_-/2)((dx_+ + dx_-)/2)} + \sigma(x, y) \frac{(T(x, y, t) - T_{+x}(x, y, t))}{(dx_+/2)((dx_+ + dx_-)/2)} \\
 & + \sigma(x, y) \frac{(T(x, y, t) - T_{-y}(x, y, t))}{(dy_-/2)((dy_+ + dy_-)/2)} + \sigma(x, y) \frac{(T(x, y, t) - T_{+y}(x, y, t))}{(dy_+/2)((dy_+ + dy_-)/2)} \\
 & \left. - Q_{mw}(x, y, t) + h_{convection}(T(x, y, t) - T_\infty)/l \right) \quad (S14)
 \end{aligned}$$

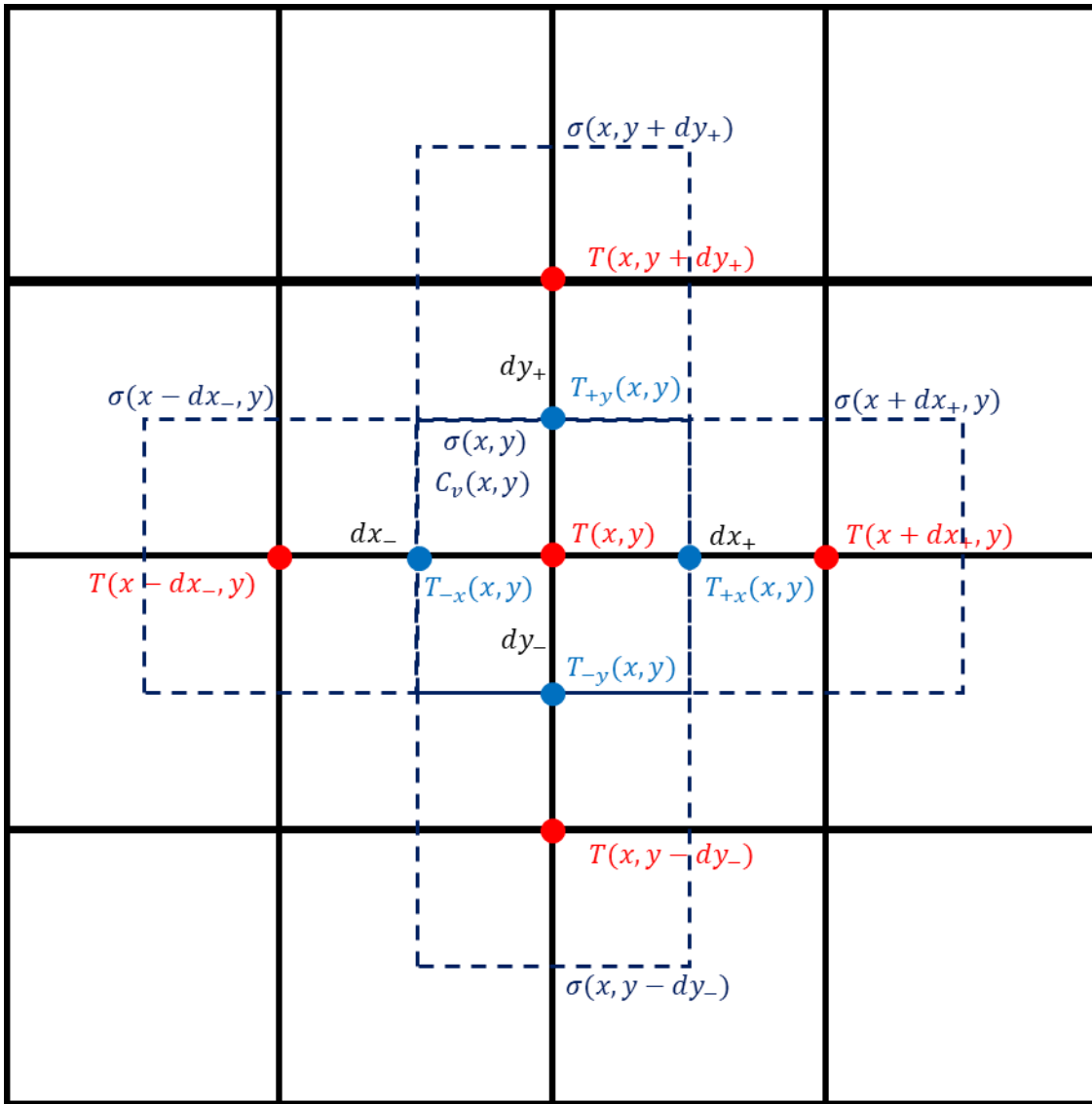
where $\sigma(x, y)$ is thermal conductivity ($\sigma(x, y) = 310 \text{ W/m}\cdot\text{K}$ for gold, $\sigma(x, y) = 0.026 \text{ W/m}\cdot\text{K}$ for air), $C_{sp}(x, y)$ is specific heat ($C_{sp}(x, y) = 0.129 \text{ J/g}\cdot\text{K}$ for gold, $C_{sp}(x, y) = 1.006 \text{ J/g}\cdot\text{K}$ for air), $\rho(x, y)$ is the density ($\rho(x, y) = 19.3 \times 10^6 \text{ g/m}^3$ for gold, $\rho(x, y) = 1.18 \times 10^3 \text{ g/m}^3$ for air), $l = 500$

nm is thickness of the gold CPW we used and the thickness of the surface we consider to simplify the thermal system into 2D, $Q_{mw}(x, y, t)$ is the surface loss density calculated using HFSS, $h_{convection}$ is the convective heat transfer coefficient, $dx(y)_{\pm}$ is the size of the cell, $T_{(\pm x(y))}(x, y, t)$ is the temperature at the boundary of the grid containing point x, y calculated as

$$T_{(\pm x)}(x, y, t) = \frac{\sigma(x, y)T(x, y, t) + \sigma(x \pm dx, y)T(x \pm dx, y, t)}{\sigma(x, y) + \sigma(x \pm dx, y)},$$

$$T_{(\pm y)}(x, y, t) = \frac{\sigma(x, y)T(x, y, t) + \sigma(x, y \pm dy)T(x, y \pm dy, t)}{\sigma(x, y) + \sigma(x, y \pm dy)}, \quad (S15)$$

and the $\pm x(y)$ notations follow the grid scheme in Supplementary Fig. S4. We used the boundary condition as $T_{\infty} = 26^{\circ}\text{C}$ to reflect the ambient condition.



Supplementary Figure S2. Grid notation used for the temperature simulation using python. The dotted line squares represent a single unit cell used in the temperature calculation.